https://ntrs.nasa.gov/search.jsp?R=19690014337 2018-07-24T06:54:14+00:00Z

General Disclaimer

One or more of the Following Statements may affect this Document

- This document has been reproduced from the best copy furnished by the organizational source. It is being released in the interest of making available as much information as possible.

- This document may contain data, which exceeds the sheet parameters. It was furnished in this condition by the organizational source and is the best copy available.

- This document may contain tone-on-tone or color graphs, charts and/or pictures, which have been reproduced in black and white.

- This document is paginated as submitted by the original source.

- Portions of this document are not fully legible due to the historical nature of some of the material. However, it is the best reproduction available from the original submission.

Produced by the NASA Center for Aerospace Information (CASI)

CR 73315

AVAILABLE TO THE PUBLIC

UNIPOLAR INDUCTION IN THE MOON AND A LUNAR LIMB SHOCK MECHANISM

K. Schwartz
American Nucleonics Corporation
1007 Air Way
Glendale, California 91201

C. P. Sonett*
Imperial College
London, England

and

D. S. Colburn
Space Science Division
NASA Ames Research Center
Moffett Field, California

N69-23715 (ACCESSION NUMBER)
(THRU)
68 (PAGES)
1 (CODE)
CR-73315 (NASA CR OR TMX OR AD NUMBER)
30 (CATEGORY)
FACILITY FORM 602

*On leave from NASA Ames Research Center

ABSTRACT

The unipolar induction mechanism is employed to calculate electric field profiles in the interior of a chemically homogeneous moon possessing a steep radial thermal gradient characteristic of long-term radioactive heating. The thermal models used are those of Fricker, Reynolds, and Summers. From the magnetic field, the magnetic back pressure upon the solar wind is found. The electric field profile is shown to depend only upon the activation energy, E_o, of the geological material and the radial gradient of the reciprocal temperature. The current is additionally dependent upon the coefficient of the electrical conductivity function but only by a scale factor. Since the moon is experimentally known to correspond to the case of weak interaction with the solar wind, the magnetic back pressure is calculated without the need for an iterative procedure. The results indicate that a hot moon can yield sufficient current flow so that the magnetic back pressure is observable as a vestigial limb shock wave using an activation energy of about 2/3 electron volts together with a conductivity coefficient of about 10^3 mhos/meter. Such matter is approximated by diabase-like composition, although the

result that both the activation energy and coefficient enter into the current determination does not rule out the possibility of a match with other similar substances. The calculations are entirely consistent with earlier results which indicated a model where the unipolar current density is dominated by a high impedance surface layer and a strong shock wave is inhibited. In addition to the magnetic back pressure, the integration of the current continuity equation permits current densities and joule heating rates to be calculated, though the magnitude of the latter for present solar wind conditions is not thermally important.

UNIPOLAR INDUCTION IN THE MOON AND A LUNAR LIMB SHOCK MECHANISM

1.0 Introduction

The presence of the solar wind together with the interplanetary magnetic field means that the moon is exposed to a motional electric field, $\vec{E}_m$, the consequence of which is that the moon develops a polarization charge field to partially cancel $\vec{E}_m$ in the interior. For an electrically conducting solar wind, the polarization charges will continually leak away. This leakage current is maintained by the charge buildup driven by $\vec{E}_m$. The system constitutes a unipolar dynamo driven by the convective energy of the solar wind and dominated by the conductivity of the moon and the solar wind. The currents which flow as a consequence of the partial neutralization of the polarization field close wholly in the solar wind, threading the moon in the process and generating a magnetic field which exerts a back pressure upon the solar wind (Sonett and Colburn - 1967, 1968). A consequence is the formation of a region of interaction ahead of the moon. However, if the surface layer of the moon is a poor electrical conductor, the formation of a strong interaction

is prevented, and no substantial shock wave is observed (Colburn et al, 1967).

The observations of Explorer 35 (Colburn et al, 1967; Ness et al, 1967; Lyon et al, 1967) support the view that the interaction with the solar wind is dominated by the stoppage of the plasma flow because of the geometrical lunar target. That the interaction is actually more complicated is attested to by the presence, sometimes, of a rarefaction wave closing the plasma deficient cavity on the downstream side of the moon. This and the enhancement of the magnetic field in the interior of the cavity were initially reported by Colburn et al (1967), who explained the rarefaction as being due to plasma diamagnetism of the solar wind against the cavity and the interior field increase as due to the tensor pressure balance.*

In addition to the primary magnetohydrodynamic interaction on the downstream side of the moon, there is occasionally observed a secondary effect consisting of small enhancements of the interplanetary magnetic field (Ness et al, 1967; Sonett and Colburn, 1968; Lyon et al, 1967), invariably lying outside (on the solar wind side) of the rarefaction.

---

*The form of the equations of motion used by Colburn et al (1967) is incorrectly reported by Ness et al (1968) to include only a perpendicular pressure term.

The small increases in magnetic field are seen only some of the time. Generally, they are so small as to tax the resolution limit of the instrument. (For details of the instrument system, see Mihalov et al, 1968.)

The observations are made downstream of the moon and thus, if attributable to an interaction of the solar wind with the moon, must be extrapolated backwards to the region close to the surface. Siscoe et al (1968) observed that the downstream plasma flow extrapolated back to the moon appears to be deviated about 3 degrees away from the solar wind flow direction and away from the moon's limb and that the density is enhanced locally. These observations, also near the limit of instrument resolution, suggest that a very weak shock wave is witnessed. Ness et al (1968) and Whang and Taylor (1968) have proposed a particle orbit theory to explain in a unified manner all magnetic observations, including the small enhancements noted here. We believe that there are potentially serious criticisms of their results; these are considered in the discussion later in this paper.

The special properties of the small perturbations are that they are always identified as field <u>increases</u>, and their position invariably lies <u>on the</u>

solar wind side of the primary cavity rarefaction. Aerodynamic reasoning suggests a lunar interaction rather than a purely plasma effect arising in the disturbed flow behind the moon. Such an interaction must arise from an exchange of momentum on the forward side of the moon (forebody) and results in a shock wave, albeit small in this case. Such a shock wave should not be confused with the wave structure studied by Michel (1967, 1968) and by Wolf (1968) which corresponds to the diamagnetic cavity closure.

A magnetogasdynamic interaction cannot be ruled out as a source for the momentum exchange but would require partial reflection of the solar wind ions at the surface. Other possibilities are sputtering of ions from the lunar surface, outgassing of the surface followed by fast charge exchange with solar wind ions, or photoionization and a substantial photoelectron pressure just above the lunar surface. All these mechanisms can be shown unlikely in one or more ways. A purely gas dynamic collisional momentum exchange between the solar wind and an outgassed surface layer seems quite unlikely in view of the extreme mean free path, even if solar wind neutral particles were admitted to the model. An interaction of the solar wind with permanently magnetized matter on the moon is possible but requires further consideration.

In a recent paper, Hollweg (1968) has explored a moon of inhomogeneous conductivity employing a two layer model. In his model the outer or crustal part has the higher conductivity based upon the possibility that subsurface ices carrying incremental contaminants could yield a higher value of conductivity than would the interior. He applies the unipolar concept and demonstrates cases where a small limb shock wave forms depending upon the particular conductivity specified.

In this paper, we also use a moon with angular symmetry but the conductivity profile is determined strictly by the dependence of conductivity of geological matter upon temperature. The moon is assumed hot and, therefore, the conductivity function will display a monotonic decrease in value from the center outward. It seems likely that either model is deficient in at least the assumption of angular symmetry especially in view of the recent discovery of mascons (Muller and Sjogren, 1968) which suggests that significant thermal differentiation has taken place. It appears likely that this would be accompanied by angular variations in conductivity. Thus, any model where it is hoped to carry out reasonable analytic calculations must be regarded as an approximation.

We apply the unipolar induction mechanism, employing a spread of conductivity functions to cover a representative range of lunar conditions and a variety of thermal models. The key question explored is whether, in the presence of the cool, poorly conducting crust, it is possible for unipolar induction to provide sufficient current so that a magnetic back pressure consistent with the observed data could occur. Although we have not explored temperatures representative of a "warm" moon -- i.e., in the 500 to 1000 degree range because of computer time limitations -- the principal conclusions would not be altered. In the course of the investigation, it is necessary to calculate the electric field profiles in the interior for the different conductivity functions. Representative cases are included as are certain current and joule heating calculations; this is done to provide a more complete assessment of the properties of the model.

The model assumes that significant permanent magnetic material with either induced or remanent magnetism is absent near the surface of the moon (Behannon, 1968). It also assumes that neither a self-excited lunar dynamo nor a permanent magnetic body of lunar scale containing remanent fields in the core region is of sufficient consequence to cause measurable solar wind back pressure. A

dynamo appears unfeasible since the lunar spin angular momentum is small, although this argument cannot be rigorously justified at the present time. Current scientific opinion does not appear to support the idea of an active dynamo, and if one exists, its external manifestation must be small since no field of a permanent nature was detected at Explorer 35 positions above some 2 gamma (Sonett et al, 1967) or on the surface above 4 gamma (Behannon, 1968). A permanent dipole at the center of the moon seems unlikely since the core would have to have passed through its Curie point at some time when the interplanetary magnetic field was substantially larger than at present. Again, this seems unlikely since the thermal time constant for the moon is sufficiently long so that the required field would have had to be present at least 1 and perhaps 2 eons after the formation of the solar system. Such a field would be inconsistent with reasonable spin damping for the sun (Weber and Davis, 1967; Modisette, 1967). Further, an initially hot moon capable of fractionating iron would still lie above the Curie point. Lastly, such an Fe-Ni core could not be very large and still preserve the proper mean density for the moon.

2.0 The Unipolar Mechanism

We assume that there is a unipolar induction generator in operation in the moon (Sonett and Colburn, 1967, 1968). The motion of the solar wind together with a non-vanishing electrical conductivity for the moon assures that the polarization electric field is partially depleted by the flow of current through the moon, while being continuously replenished by the motional electric field. Details of the mechanism are given in the referenced papers together with electric field profiles for hot moons composed of olivine.

In this paper, the earlier assumptions regarding spherical symmetry of the moon with respect to both the interior and exterior electrical conductivity and cylindrical symmetry for the current are maintained. That these are oversimplifications is evident from Explorer 35 results, and the effects of the lunar cavity will tend to decrease the efficiency of the system. The basic mechanism is valid although azimuthal symmetry is destroyed.

The vector product of the moon's velocity and the local magnetic field produce a motional electric field, $\vec{E}_m = \vec{V} \times \vec{B}$, in the moon's rest frame. Here $\vec{V}$ is the moon's apparent velocity with respect to the solar

wind and $\vec{B}$ is the net magnetic field measured at the moon. Because of its high conductivity, the solar wind plasma acts as brushes to complete the current path through the moon. No current paths are permitted to close within the moon itself in the steady-state. The natural coordinate system is spherical, centered in the moon, and set up with colatitude, θ, measured from the direction of $\vec{E}_m$.

3.0 Boundary Value Problem

For the steady interaction, the current continuity condition is given by

$$\nabla \cdot \vec{J} = 0 \tag{1}$$

where $\vec{J}$ is the current density.

3.1 Assumptions

For mathematical tractability, the following assumptions are made:

a) The currents exhibit azimuthal symmetry, $\frac{\partial}{\partial \varphi} \equiv 0$ within the moon.

b) The current density is related to the electric field through a conductivity function σ dependent upon temperature alone.

c) The temperature is a function of the radius only; i.e., the moon possesses a radially symmetric thermal profile.

d) The prescribed tangential electric field at the moon's surface is given by

$$\vec{E}_T = -\hat{e}_\theta \left| \vec{V} \times \vec{B} \right| \sin \theta \tag{2}$$

where $\hat{e}_\theta$ is the unit vector in the direction of increasing θ. (The free stream value for $\left|\vec{V} \times \vec{B}\right|$, using nominal solar wind values, produces a motional field of 2.8 millivolts/meter.)

e) The effect of the back pressure of the induced field upon the solar wind is accounted for heuristically by a pure number, k, where $0 \leq k \leq 1$ (Sonett and Colburn, 1967). The value of k is determined by balancing the incident solar wind pressure against the induced magnetic field pressure of the unipolar generator. For a very weak interaction, $k \to 0$, while at the other limit, for a strong interaction, $k \to 1$. In this paper the k factor is determined from solutions to Eq. (1). The solutions for the field and current density are then reduced by $(1 - k)$. The k factor is thus a measure of the deviation of the solar wind around the moon, the deviation being caused by the back pressure on the solar wind of the induced magnetic field.

3.2 Solutions

Under the restrictions of Section 3.1, and since $\vec{B} = 0$, we find that $\vec{E} = -\nabla\psi$ and Eq. (1) becomes

$$\sigma\nabla^2\psi + \sigma'(r)\ \psi'(r) = 0 \qquad (3)$$

where the prime denotes differentiation with respect to the indicated argument. With the definition*

$$\psi(r,\theta,\varphi) = R(r)\Theta(\theta)\Phi(\varphi) \qquad (4)$$

Eq. (3) can be separated into the differential equations

$$R'' + \left(\frac{2(n+1)}{r} + \frac{\sigma'(r)}{\sigma}\right)r' - \frac{n(n+1)\ R(r)}{r^2} = 0 \qquad (5a)$$

$$(1-u^2)\ \Theta'' - 2u\Theta' + \left[n(n+1) - \frac{m^2}{1-u^2}\right]\Theta = 0 \qquad (5b)$$

$$\Phi'' + m^2\ \Phi = 0 \qquad (5c)$$

with constants of separation, n, m, and where $u = \cos\theta$. The general solution to the system of differential equations given by Eqs. (5a), (5b), and (5c) is

*The validity of Eq. (3) rests upon the assumption that $\sigma=\sigma(r)$ alone. Joule heating (see Section 7.0) is cylindrically symmetric and actually $\sigma=(r,\theta)$. However, the θ dependence is small and only very small errors are introduced into σ by ignoring the angular dependence.

$$\psi(r,\theta,\varphi) = \sum_{m,n} A_{mn} \left(\frac{r}{a}\right)^n Q_n\left(\frac{r}{a}\right) P_n^{|m|}(\cos\theta) e^{im\varphi} \tag{6}$$

where a is the lunar radius (taken as 1740 km), $P_n^{|m|}(x)$ is the associated Legendre Polynominal of order m, n, and $Q_n(x)$ is a solution of the differential equation

$$xQ'' + \left[2n+2 + x\gamma(x)\right] Q' + n\gamma(x)\, Q(x) = 0 \tag{7}$$

which is obtained from Eq. (5a) by the substitutions

$$x = r/a \tag{8a}$$

$$R(ax) = x^n Q_n(x) \tag{8b}$$

and

$$\gamma(x) = a\sigma'(ax)/\sigma(ax) \tag{8c}$$

The coefficients A_{mn} are determined from the boundary conditions on the field at r=a (x=1). From the boundary conditions and assumptions a and d, only the n = 1, m = 0 term is required for the solution:

$$\psi(r,\theta) = -\left|\vec{V} \times \vec{B}\right| \left(\frac{r}{a}\right) Q\left(\frac{r}{a}\right) \cos\theta \tag{9}$$

The function $Q(\frac{r}{a})$ has been obtained for various conductivity functions on a CDC 6600 digital computer.

3.3 The Coupling Term

We consider conductivity functions having the general form

$$\sigma(T) = \sigma_o \, e^{-E_o/kT} \tag{10}$$

(Runcorn, 1956; Rikitake, 1966; Parkhomenko, 1967) where σ_o is the conductivity for $T = \infty$ (a mobility-like parameter), E_o is the activation energy; k, Boltzmann's constant; and T, the temperature. For this type of conductivity function, the coupling term of Eqs. (5a) and (7) reduces to

$$\frac{\sigma'}{\sigma} = \frac{1}{\sigma}\frac{d\sigma}{dT}\frac{dT}{dr} \rightarrow \frac{E_o}{kT^2}\frac{dT}{dr} = \frac{E_o}{k} \cdot \frac{d}{dr}\left(-\frac{1}{T}\right) \tag{11}$$

Eq. (11) is independent of the coefficient, σ_o and the coupling term σ'/σ, depends only upon the activation energy E_o and the gradient of reciprocal temperature. The coupling term may alternatively be regarded as measuring the volume density of charge in the lunar interior.

As Eq. (6) is intrinsically independent of σ_o, the electric field in the interior depends only upon the

activation energy, E_o. However, for the hypothetical case where a strong interaction existed, the current density interated over the whole moon would yield so great a back pressure upon the solar wind that the net motional field, E_m, would be reduced. Thus, though Eq. (6) shows no direct dependence upon σ_o, electric field distributions independent of σ_o must be regarded as corresponding to the case of a weak interaction where $k \ll 1$. For the case where $k \sim 1$, the electric field distribution in the interior is scaled down by the factor $(1-k)$. The appropriate factor, k, is determined from solutions to Eq. (6) and calculation of the net magnetic back pressure generated. Finally, the results for the empirically indicated moon (lacking a strong bow shock) are that the electric field distribution is functionally determined by E_o alone, but that the presence of a vestigial limb wave must be jointly given by E_o and σ_o.

4.0 Trial Conductivity Functions

It is almost certain that the assumption of a chemically homogeneous moon is unreal; however, it does permit construction of conductivity models dependent only upon temperature and therefore allows rational computational tests for the induction hypothesis to be carried out.

The choice of candidate materials from which to construct conductivity profiles is based upon the aim that a spread of final conductivity profiles be available for insertion into the computer program. We include olivine to permit identification with earlier calculations (Sonett and Colburn, 1967). The nomenclature used for the other materials is at best a useful representation, and it is likely that specific samples of minerals could be found which might deviate from the sample functions used here.

Actually, the conductivity of olivine-like minerals depends strongly upon Fe^{++} and Fe^{+++} substitution for Mg; in the pure state, olivine is rather an insulator (Shankland, 1968). Therefore, the terminology used here, although following strictly from empirical measurements, should be regarded only as a classification aid for Eqs. (11a, b, c, d). The first three functions, Eqs. (11a, b, c),

represent only the impurity or low temperature mode. The addition of the two higher temperature modes, intrinsic electronic and ionic, would lead to an enhancement of conductivity in the core of the moon. For a hot moon, the core already forms an electrical short circuit due to the leading term of impurity conduction. Such a shorting section has little electrical effect except to enter into the calculation of the total potential drop across the moon; therefore, we ignore the intrinsic electronic and the ionic terms.

The total current is most dependent upon the outer, cooler, and more resistive part of the moon; i.e., the crust. It is for this reason that the low temperature or impurity conductivity provides the leading effect. Eq. (11d) reflects the earlier work on unipolar induction and contains the additional two parts of the total thermal conductivity function for completeness. The conductivity functions are all characterized by the mobility, σ_o, and activation energy, E_o, as before in Section 3.3. They are given analytically by the expressions*

Peridotite: $\sigma_p(T) = 1.26 \times 10^5 \exp(-.655/\xi T)$ (12a)

*Eqs. (12a, b, c) are determined from experimental data given by Parkhomenko (1967). Eq. (12d) is a representative olivine from Rikitake (1966). Eq. (12c) is an average over several cases.

Diabase: $\sigma_D(t) = 10^3 \exp(-.634/\xi T)$ (12b)

Basalt-Diabase: $\sigma_{BD}(T) = 130 \exp(-.78/\xi T)$ (12c)

Olivine: $\sigma_{OL}(T) = .01 \exp(-.5/\xi T)$

$+ 10 \exp(-1.64/\xi T) + 10^5 \exp(-3.02/\xi T)$ (12d)

where $\xi = 8.6176 \times 10^{-5}$ electron volts/°K.

The four conductivities are shown graphically in Figure 1 where the logarithm of the conductivity is plotted against 1000/T. The olivine function is dominated by its leading term at temperatures below 1200°K. (It is shown later that the dominant effect from the conductivity coupling occurs at low temperatures where the thermal gradient is greatest, and this takes place near the lunar surface.) Eq. (12c) has the greatest variation with inverse temperature and peridotite and diabase functions the least. The olivine function has the least change with temperature below T = 1200°K. In addition to the four conductivity functions given by Eqs. (12), we shall include one additional function, σ_M, in order to emphasize the effect of changing σ_o without modifying the activation energy, E_o. If the interaction is weak so that the induced current produces little or no reaction back on the solar wind

($k \ll 1$), the electric field should be nearly identical for two different conductivity models differing by only the value of σ_o. To investigate this point in detail, we obtain the fields and currents associated with the conductivity function

$$\sigma_M = 100 \exp(-.634/\xi T) \tag{12e}$$

found by scaling the coefficient σ_o in Eq. (12b) downwards by a factor of 10. We denote σ_M as a modified diabase function for convenience. The electric field, current densities and joule heating will then be compared for the solution of Eq. (9) derived for both σ_D and σ_M.

5.0 Lunar Thermal Profiles

As the electrical conductivity and therefore the total induction rests eventually upon the thermal profile of the moon, an analytic form for the latter is needed for incorporation into the computer code. For this, we use the profiles developed by Fricker, Reynolds, and Summers (1967) for various radionuclide concentrations and genetic starting temperatures for the moon. The Fricker, Reynolds, and Summers (hereafter referred to as FRS for brevity) models used are their numbers 5, 6, 7, and 8. For a detailed explanation of the models and the methods by which they obtained their results, the reader is referred to the above article and also to Reynolds, et al (1966). The thermal profiles are characterized by a common melting curve, and used two radioactive material mixes for heating, one being that of a chondritic meteorite, the other of "terrestrial" material.

Model 5 starts with an initially cold (0°C) moon and uniformly distributed "chondritic" radioactivity. Models 6 and 7 use "terrestrial" radioactivity, Model 6 being initially hot in the center and going to 0°C at the surface, while Model 7 is initially a uniform 500°C. Model 8 is also initially a uniform 500°C but with "chondritic" heat sources. Each of the four models

results in an identical thermal profile from the center of the moon out to 1100 kilometers. In Figure 2, the thermal profile for Model 5 is shown as representative of the group. The scale precludes observation of small differences which exist in the outer part of the moon. These differences can be seen in the representation of Figure 3 which gives the region under the surface in expanded form. FRS Model 5 has the smallest subsurface gradient, $\sim 4.2°C/km$, Models 7 and 8 show $\sim 6°C/km$, and the largest gradient is displayed by Model 6 having $\sim 7.0°C/km$. The behavior of the solutions depends ultimately upon these subsurface gradients. The final physical effects can be attributed to the thermal profile over the outer 10 to 20 km just under the surface of the moon.

6.0 Numerical Results

The electric field within the moon derived from Eq. (5) can be written in the form

$$\vec{E}(r,\theta)/\left|\vec{V} \times \vec{B}\right| = \hat{e}_r R'(r) \cos\theta - \hat{e}_\theta \frac{R(r)}{r} \sin\theta \qquad (13a)$$

where $\hat{e}_r$, $\hat{e}_\theta$ are unit vectors in a spherical polar system with customary convention. The value of $E(r,0)$ is given by $\left|\vec{V} \times \vec{B}\right| R'(r)$ and of $E(r,\pi/2)$ by $-\left|\vec{V} \times \vec{B}\right| R(r)/r$. The field profile over the whole moon can be obtained from Eq. (13a); for the present problem examination of the field at $\theta = 0$ and $\pi/2$ is adequate. The magnetic field in the moon, $\vec{H}$, produced by the unipolar generator, is given by

$$\vec{H} = \hat{e}_\varphi \left|\vec{V} \times \vec{B}\right| \frac{ar}{2} R'(r)\sigma(r)\sin\theta \qquad (13b)$$

where a is the radius of the moon (1740 kilometers).

The two components of the electric field have been obtained for various combinations of the conductivity functions given in Section 4.0 and the thermal profiles given in Section 5.0. The results are divided into three parts. In the first, we investigate the effects produced on the solution for the electric field when the conductivity

function is fixed but the thermal profile is varied. For the calculation, the conductivity function given by Eq. (12d) is employed. In the second part, the thermal profile is held fixed using FRS Model Number 5. The effect caused by changing the temperature dependence of the conductivity is there investigated.

Finally, we compare the electric field current density and heating rates for the two conductivity functions given in Eqs. (12b,e) in conjunction with FRS thermal profile Number 5.

6.1 Fixed Conductivity Function (Olivine) with Variation of Thermal Profile

In Figure 4, the electric field is plotted as a function of depth below the lunar surface in the equatorial plane, $\theta = \pi/2$ for all four FRS models. The olivine conductivity function, Eq. (12d), is used to calculate the coupling term in Eq. (5a). Attention is directed to the tangential field at the surface, $r = a$, which for all four thermal profiles is identically the free stream field, 2.8 millivolts per meter. This is a consequence of the boundary condition on E_t together with the infinitesimal interaction leading to an extremely small k factor when employing the olivine conductivity function ($k \sim 10^{-8}$). Further, it is found

that the field distribution near the surface is identical for Models 7 and 8. This is a consequence of the two profiles being identical over the 150 kilometers just below the surface. Model 5 has the smallest thermal gradient and accordingly has the smallest gradient of the electric field in the equatorial plane. Progressively greater thermal gradients produce greater electric field gradients. If the temperature, and therefore the conductivity, had been constant, the electric field would have exhibited a constant value of 2.8 millivolts per meter throughout the moon, provided that $k \ll 1$.

In Figure 5, the electric field along the polar axis ($\theta = 0$) is plotted as a function of depth below the surface for four thermal profiles and an olivine conductivity. The field values are consistently higher than in Figure 3 by some three orders of magnitude. The thermal gradient produces a buildup in the electric field near the lunar surface at the poles and the profile with the largest thermal gradient produces the largest value of the electric field at the surface. The gradient of this electric field component again increases with increasing thermal gradient. The three curves cross approximately 2.5 kilometers below the surface.

In the region of special interest just under the surface, the thermal gradient can be approximated by

a constant. Therefore the coupling term in Eq. (5) is constant over this part of the interior. The results for the electric field in the equatorial plane show increasing gradient as the coupling term grows due to an enhanced thermal gradient while holding the activation energy fixed. The situation for the polar electric field is more complex. Here a cross-over is noted at about 2 km under the surface, but the trend noted for the equatorial field is still seen. The gradient in the electric field increases with the increasing thermal gradient.

6.2 Thermal Profile 5 - Variation of Conductivity

In Section 6.1, we showed the effects which are obtained for four models of the moon which have a hot interior and cold (0°C) surface. For that discussion, a model conductivity function was used which provides a very poorly conducting surface layer ($\sigma \sim 6 \times 10^{-12}$ mhos/meter). In this section, we fix the thermal profile (Model 5) and examine the effects of using different conductivity functions for the lunar model.

In Figure 6, the electric field is plotted as a function of depth for $\theta = \pi/2$. The curves obtained for the olivine, diabase, and basalt-diabase conductivity functions all start at the free stream value of 2.8

millivolts/meter. They exhibit increasing electric field gradients corresponding to the increasing value of the activation temperature, E_o/k in the conductivity function given in Eqs. (12a, b, c, d). The one anomalous curve was obtained using the peridotite function. The tangential field obtained for this function at $r = a$ is only 1 millivolt/meter. This decrease of approximately 70% from the free stream field is an indication of a strong moon-solar wind interaction. For this particular model calculation, k factor = 0.7; 70% of the solar wind and the embedded solar magnetic field are swept around the limb of the moon, and E_m is reduced by 70%. The electric field distribution in the polar direction ($\theta = 0$) is shown in Figure 7. The field behavior in this case is similar to that shown in Figure 5. In Figure 5, the results are modified by variations of the temperature profile from one thermal model to another. The differences are traced to the functional differences in the behavior of the electrical conductivity with temperature using a common thermal profile. As in Figure 6, the curve for peridotite is substantially below the other three curves because of the large k factor. The results found in Section 6.1 for the variable thermal profile and fixed conductivity function are repeated qualitatively in the present calculation. This is expected since the coupling term σ'/σ

consists of the product of the activation energy and the gradient of the temperature, and variation in either should have the same general effect. The similarity is carried over even into the polar fields where the same cross-over phenomenon is noted.

6.3 Thermal Profile 5 - Diabase and Modified Diabase Conductivities

For the two conductivity functions, Eqs. (12b, e), and the Model 5 thermal profile, $k = 2.75 \times 10^{-3}$ for the diabase conductivity function and 2.77×10^{-5} for the modified diabase function. From the definition of E_m, these small values of k mean that the electric fields calculated from the same thermal profile with the two different conductivity functions should differ from each other by approximately .275%, with the electric field E_m for the modified conductivity being larger. The numerical calculations bear out this prediction. The computed differences vary from .269% to .280%. The electric field profiles are shown in Figure 8 for $\theta = 0$ and $\theta = \pi/2$. Because of the scale, the difference between the two cases is indistinguishable. The solutions were obtained for a free stream field of 2.82 millivolts/meter. In the deep, hot interior of the moon, both field terms are approximately 3×10^{-10} volts/meter. Near the surface,

the field in the equatorial plane ($\theta = \pi/2$) increases to the free stream value. Along the pole ($\theta = 0$), the field increases to 2 volts/meter, greater by a factor of 700 than the free stream motional electric field.

7.0 The Electric Field Profile in the Interior

In Section 6.0, the electric field was computed in the interior of various hot moons; the computation was restricted to the angular values $\theta = \frac{\pi}{2}$, the electrical equator, and $\theta = 0$ along the pole. In these two cases the field is respectively normal to the equator ($E_r = 0$) and radial ($E_\theta = 0$).

7.1 The Field When $E_r = 0$

On the electrical equator, the field, $\vec{E}$, is everywhere tangential to the surface and the boundary condition requires continuity of $\vec{E}$. For the cases in vestigated in this paper, this condition reduces to the requirement that the free stream plasma field and that in the interior should match. Both Figures 4 and 6 confirm this for all but peridotite. In the latter case the condition $k \ll 1$ no longer holds and the interaction is strong. The field, E_m, is reduced to approximately 1 millivolt/meter. This interpretation is supported by the value of k computed in Section 9.0 where an approximate perturbation field is found. The perturbation field is inexact since the undeviated value of E_m is used for the determination of k which should then be iterated to determine a better value of E_m (Sonett and Colburn, 1967, 1968). Since the moon does not display a strong interaction, our approximation is sufficient.

In all the cases shown, both for variation in T and in E_o (the latter holding the temperature profile fixed; i.e., Model 5 of FRS), the coupling term

$$\sigma'/\sigma = \frac{E_o}{k} \frac{d}{dr} \left(-\frac{1}{T}\right)$$

of Eq. (5) results in an internal electric field which depends on position. This is indicative of the positionally dependent potential drop in the interior arising from the inhomogeneity of the electrical impedance.

7.2 The Polar Field (E_θ=0)

Here the boundary condition requires only that the current density, σE, be continuous. This is implicit in the form of the field given by Eq. (13a) because we assume that the plasma conductivity is high compared to the lunar conductivity. Along the line through the poles (E_θ=0) the net potential drop depends only upon the free stream field and the lunar diameter. A variable conductivity as in the present problem results in an inhomogeneous electric field, but the total potential drop is conserved. The electric field in the deep interior is diminished to a small value, assuming a moon where the interior conductivity rises, and the result is that the

electric field near the surface must rise to a high value (Sonett et al, 1968).

Approximate values of the coupling constant, σ'/σ, are shown in Table 1 for the four thermal profiles and for three of the compositions. The gradient of reciprocal temperature $d(1/T)/dr$ is nearly the same for FRS Models 6, 7, and 8 equaling 1.8×10^{-5} (deg-km)$^{-1}$ and has twice the value or 3.46×10^{-5} (deg-km)$^{-1}$ for Model 5. As the coupling constant is the product of the two factors, one depending upon activation energy and the other upon the thermal profile, the two have equal weight in determining the local electric field and the volume charge density, ρ_v, obtained from the equation

$$\nabla^2\psi = -\frac{\psi'(r)\sigma'(r)}{\sigma} = -\frac{\rho_v}{\epsilon} \qquad (14)$$

which comes directly from Eq. (3).

Reference to Table 1 shows that a monotonic trend exists in the value of coupling constant, increasing from olivine, diabase, and finally basalt-diabase. The associated electric fields indicate that the electric field confirms the importance of the gradient of the conductivity near the surface (Figures 5 and 7). The cross-over is due to the additional constraint

	Substance		
	Olivine	Basalt-Diabase	Diabase
Models 6,7,8			
$\frac{d}{dr} - (\frac{1}{T}) = 1.8 \times 10^{-5} (\text{deg-km})^{-1}$	0.105	0.163	0.132
Model 5			
$\frac{d}{dr} - (\frac{1}{T}) = 3.46 \times 10^{-5} (\text{deg-km})^{-1}$	0.20	0.313	0.255

Table 1 - Coupling Constant, $\frac{\sigma'}{\sigma}$ (volts/m^2), for Varying Composition and Thermal Profile

that the to[illegible]otential drop across the moon is constant. Thus Model 6 shows the largest value of σ'/σ and the largest electric field until the cross-over.

8.0 Currents and Joule Heating

The current density, $\vec{J}$, is obtained by multiplying $\vec{E}$ by $\sigma(r)$. Since σ_D is greater than σ_M by a factor of 10, the current densities for these two examples should differ by just this factor. Current densities shown in Figure 9 for the equatorial plane $\theta = \pi/2$, and the pole, $\theta = 0$. The current densities for the two cases are displaced from each other by a factor of 10, but are otherwise indistinguishable. The current density on the equator ($\theta = \pi/2$) is less for $r = a$ than the polar value by a factor of 700.

The heating rate expressed in joules/meter^3-sec. is given by

$$H = \vec{j} \cdot \vec{E} = \sigma(\vec{E} \cdot \vec{E}) = \sigma E_m^2 \left[(R' \cos \theta)^2 + (R \sin \theta / r)^2 \right]$$

$$= \dot{H}_r + \dot{H}_\theta \qquad (15)$$

The two heating rates represented by $\dot{H}_r$ and $\dot{H}_\theta$ are direct consequences of the earlier assumption of separability based upon $\sigma = \sigma(r)$ alone. It is possible to test the symmetry and separability assumptions of Eq. (3) by computing the heating rate using either of the values; we have carried this out and find that the

difference is small confirming the general validity of separability. The heating terms can be separately written as

$$\dot{H}_r = \sigma E_m^2 (R' \cos \theta)^2 \tag{16a}$$

and

$$\dot{H}_\theta = \sigma E_m^2 \left(R \frac{\sin \theta}{r}\right)^2 \tag{16b}$$

The joule heating rate is now obtained for the diabase and modified diabase conductivity functions using FRS Model 5 for the thermal profile. No iteration is required in this calculation since the effect of induction using present day solar wind parameters is too small to have added a significant non-radionuclide fraction to nuclear heating in the past. The joule heating rate is shown in Figure 10 for both the normal and modified conductivities for diabase. The results differ by just the ratio $\sigma_{od}/\sigma_{dm} = 10$. The heat rate of 8×10^{-9} watts/m^3 translates to approximately 8×10^{-8} joules/gram-year at the lunar surface.

9.0 The Induction Magnetic Field

The calculation of the current through the moon now permits an evaluation of the magnetic field due to the induced current system. The calculations are restricted to FRS Model 5 and a range of conductivities. This permits a direct test of the original hypothesis that the secondary field enhancements are a consequence of induction. Since the magnetic field varies as sin θ, this test extends to all latitudes.

The magnetic field at the lunar surface is derived from Eq. (13b)

$$H_{\varphi} = \left| V \times B \right| \frac{a^2 R'}{2} (a)\sigma(a)\sin\theta \qquad (17)$$

The results are most conveniently expressed in terms of the factor k which is a representation of the deviated flow. Figure 11 shows the logarithm of the induction field plotted against k with the field expressed in units of gamma (1 gamma = 10^{-5} gauss). The maximum field perturbation occurs for peridotite. A conductivity function with E_o = 0.634 ev. and $\sigma_o = 10^3$ mhos/meter provides a magnetic field of the correct order to match the experimental results. The calculation of the perturbation field necessarily includes the coefficient σ_o, as seen in Eq. (17) since $\sigma(a) = \sigma_o \exp\left\{-E_o/\xi T(a)\right\}$. At the

other end of the scale, results from the olivine and basalt-diabase are so small as to produce surface magnetic fields which are well below detectability by present instrumentation and would produce no detectable solar wind interaction. For diabase, this model yielded a field of 3 gammas. A magnetic field of this size will produce sufficient pressure to balance the normal component of the solar wind pressure, starting at approximately 3° from the limb of the moon.

The straight line relation of Figure 11 between the intensity of the magnetic field perturbation and the value of k is a direct consequence of the manner in which k was defined by Sonett and Colburn (1968);

$$kP_{SW} = (1-k)^2 P_H \tag{18}$$

where P_{SW} is the momentum flux of the solar wind and P_H is the magnetic field back pressure $\mu H^2/2$. In Figure 11, the quantity $\log \left|(1-k)H\right|$ is plotted against $\log k$. The quantities P_{SW} and $\mu/2$ determine the intersection at $k = 1$, $\log k = 0$.

For the three cases given by Eqs. (12a, b, c), the primary difference of these functions is in the value of the coefficient, σ_o, and the slope governed by E_o is

relatively constant as attested to by Figure 1. Thus, changes in the magnetic field are given by scale factors; σ_o and k have common roles in relation to the magnetic field and the abscissa in Figure 11 can be replaced by an equivalent σ_o for the cases where E_o varies little. The limiting case of peridotite indicates the formation of a shock wave as $k \rightarrow 1$. This requires an extensive iteration; however, this case is not significant to the main problem, as the moon is represented by the case $k << 1$. The actual case implies that saturation of the current system is approached (Sonett and Colburn, 1967).

In Figure 8, it was shown that the olivine moon model produces a magnetic field interaction which was ten times greater than the basalt-diabase model for the same profile. The lunar conductivity profiles for the Model 5 thermal profile are plotted in Figure 9 for the lunar olivine and basalt-diabase conductivity functions. Over most of the lunar volume, the basalt-diabase model has a higher electrical conductivity by a factor of 10^3. The two profiles cross at approximately $r = 1724$ kilometers, 16 kilometers below the surface. The olivine model surface conductivity is 6×10^{-12} mhos/meter, the basalt-diabase 5×10^{-13} mhos/meter. The magnetic fields and currents are in the same ratio as the surface conductivity, thus emphasizing the

importance of the low conductivity surface layer over the high internal conductivity.

10.0 Discussion

The calculations show that a moon possessing a hot interior together with representative geological matter can yield a current system substantially sufficient to explain the magnitude of the occasional limb perturbations seen by Explorer 35. As a strong bow wave is absent, the lack of an iterative procedure in calculating the expected perturbation is justified, because the net motional electric field, E_m, which enters into the calculation is hardly modified.

The form of the unipolar induction equation shows that the coupling term σ'/σ can be regarded as the product of two factors, one being the activation energy, E_o, of the matter, and the second being the radial gradient of the reciprocal temperature. Thus, the approximation of a constant thermal gradient in the outer part of the moon yields an almost constant value of coupling constant there, a fixed volume density of electrical charge, and, lastly, an approximately constant value of electric field divergence. Thus, the problem can be classified by the two parameters, and the constant, σ_o, is ignorable in the determination of electric field.

It is unlikely that the moon is compositionally as homogeneous as the model supposes; the model should

be regarded as a first order approximation to the real case where thermal inhomogeneities possibly have resulted in the development of strong compositional differences which require the addition of an angular dependence. Although the computations fit best to a diabase-like conductivity, it is clear that the basic parametrization is via the coupling constant and this depends upon the thermal profile and the activation energy.

Our earlier interpretation of the lack of a lunar bow wave was based upon the thermal profile which must exist in a hot planetary body. Even if the interior is hot, the surface, if in equilibrium with space, must be at a reasonably low temperature. Solar insolation cannot provide sufficient heat to basically alter this. The thermal wavelength, determined by the effective rotation rate of the moon with respect to the sun restricts the effective depth of insolation to less than a few meters at most. Thus the surface must be of low conductivity, and it is this fact which prohibits the formation of a shock wave. In our interpretation, since the shock is a manifestation of induction resulting in a magnetic field capable of nearly stopping the solar wind, any impediment to the currents passing through the surface of the moon into the solar wind must decrease the possible strength of the shock wave. Our calculations

show that a bow wave cannot hope to form for any thermal regime in balance with the effective black body temperature of the interplanetary cavity, unless a pathological conductivity function were chosen. The calculation does show that even an extremely small interaction can be produced by reasonable conductivity parameters. The interaction in the case of diabase is so small that only approximately 10^{-3} of the incident plasma is deviated. The magnetometer can detect the corresponding small or infinitesimal shock wave because the back pressure required can take on vanishingly small values when the shock wave forms just ahead of the terminator. The shock is extremely oblique and the normal component of pressure is lessened by $\cos^2 x$ where x is the angle from the stagnation point to the shock connection with the moon, i.e., nearly 90 degrees.

It is possible to explain the vestigial perturbation by other conductivity profiles, such as Hollweg has shown, where the crustal conductivity dominates the interior value so that nearly all the current flows in the crust. However the strong evidence for extensive thermal working of the moon implies a hot interior. Thus for a superficial layer to carry the currents requires an even more complicated conductivity profile than either the model of Hollweg or this paper. The hot

interior, together with a strongly conducting crust, means that the conductivity dependence upon radius would be non-monotonic with a significant dip or decrease at some depth in the interior. Present evidence cannot provide a choice between these models.

As the experimental perturbations seen by Explorer 35 are noted downstream and at a distance from the moon of several lunar radii, it is clear that extrapolation of their exact magnitudes to the surface is difficult at best, requiring knowledge of the Mach angle. Although the Mach angle itself can be guessed for a weak shock, the angle from the terminator at which the wave separates from the moon is unknown, and, therefore, the strength of the shock unknown.

Using an alternative model, Ness et al (JGR 73, 3421, 1968) state that for the case of B perpendicular to the solar wind velocity their model of the cavity interaction predicts exterior field increases and propose that, except for the approximate nature of the model, it should generally predict these increases. Actually the case cited does not support this confidence since the exterior increases cited (bottom of their Figure 11) appear to be part of the oscillatory artifacts that appear in several other of their cases. The explanation for the artifacts lies in the Fourier analysis computational

method used by Whang for these calculations (Whang, Phys. Fluids, 11, 1713, 1968). His vector potential A from which the field is calculated is computed over a plane containing the velocity and field using polar coordinates. The azimuthal variation at a given radius is computed by a Fourier sum of cosine $n\theta$ and sine $n\theta$ terms in which n is allowed to range from 0 to 20. Such a truncated Fourier syntheses will, of course, respond to transients by ringing at the highest frequency or, in this case, smallest angle. Consequently, any oscillatory behavior with peaks separated by 18 degrees (360/20) is suspect. The example cited (Figure 11c) shows the two exterior maxima to be separated by approximately 54 degrees with two maxima inside the cavity so that a peak appears approximately every 18 degrees. Two other attenuated peaks appear to the left of these four in the appropriate positions. Figure 11b shows the same pattern, but attenuated as is appropriate, since the cavity edge which would be the driving function has a longer rise time. In their Figure 10, 5 cycles at approximately 18 degree periods are seen in both graphs, so that for the top graph, taken at 4.5 lunar radii, only one peak occurs in the shadow but for the bottom graph, at 2.5 lunar radii, two peaks are encompassed by the shadow.

Similarly, their Figures 12 and 13 show 6 other cases in 5 of which the 18 degree oscillations are evident, the shadow encompassing 3 peaks at 2 lunar radii and 1 peak at 4 lunar radii. In Whang's presentation (op cit) the effect is also apparent. In Figure 1 minor lobes are seen approximately 18 degrees apart. In Figures 4, 6, and 7 several more 18 degree oscillations are seen, although since a rectilinear plot is used they are not equally spaced along the Y axis. It is shown in Figure 7 that the "field anomalies increase as the beta value increases". However, one must note that the rise time at the cavity edge also increases with beta, and it is this rise time that is the driving function for the Gibbs phenomenon in a low pass filter.

Thus, for any distance from the moon's center, the resolution of the computations is limited to the number of 18 degree segments contained in the cavity. Consequently, for 2 lunar radii distance, 3 peaks are found in the cavity, while for distances greater than 6 lunar radii, only a fraction of an 18 degree segment can be contained in the cavity and the solutions show very broad cavity boundaries. It remains to be demonstrated whether a finer Fourier analysis might demonstrate the independence of fields in the exterior domain, outside the Mach cone, from the density minimum which characterizes

the cavity. This seems unlikely because the density in the model goes through a simple minimum.

It must also be pointed out that the model is for a cylindrical moon, so that at distances greater than 2 lunar radii from the moon's center the edge effects from the top and bottom of the moon should cause considerable difference between the actual case and the model.

Acknowledgments

One of us (CPS) is indebted to the Guggenheim Foundation and to NASA for support and to J. W. Dungey and Imperial College for their hospitality. Support for (KS) was provided under Contract No. NAS-2-4026.

REFERENCES

1 - Behannon, K.W., "Intrinsic Magnetic Properties of the Lunar Body," JGR 73, 7257 (1968).

2 - Colburn, D.S., R.G. Currie, J.D. Mihalov and C.P. Sonett, "Diamagnetic Solar Wind Cavity Discovered Behind the Moor Science 158, 1040 (1967).

3 - Fricker, P.E., R.T. Reynolds and A.L. Summers, "On the Thermal History of the Moon," JGR, 72, 2649, May 1967.

4 - Gold, T., "In the Solar Wind," ed. R.J. Mackin, Jr. and M. Neugebauer, Pergamon Press (1966).

5 - Hollweg, J.V., "Interaction of the Solar Wind with the Moon and Formation of a Lunar Limb Shock Wave," JGR 73, 7269 (1968).

6 - Jchnson, F. and J.E. Midgley, "Note on the Lunar Magnetosphere," JGR, 72, 6113 (1967).

7 - Lyon, E.F., H.S. Bridge and J.H. Binsack, "Explorer 35 Plasma Measurements in the Vicinity of the Moon," JGR, 72, 6113 (1967).

8 - Michel, F.C., "Shock Wave Trailing the Moon," JGR, 72 5508 (1967).

9 - Michel, F.C., "Magnetic Field Structure Behind the Moon," JGR, 73, 1533 (1968).

10 - Mihalov, J.D., D.S. Colburn, R.G. Currie and C.P. Sonett, "Configuration and Reconnection of the Geomagnetic Tail," JGR, 73, 943 (1968).

11 - Modisette, J.F., "Solar Wind Torque on the Sun," JGR, 72, 1521 (1967).

12 - Muller, P.M. and W.L. Sjogren, "Mascons: Lunar Mass Concentrations," Science, 161, 680 (1968)

13 - Ness, N.F., K.W. Behannon, C.S. Scearce and S.C. Cantarano, "Early results from the Magnetic Field Experiment on Lunar Explorer 35," JGR, 72 5769 (1967).

14 - Ness, N.F., K.W. Behannon, H.E. Taylor and Y.C. Whang, "Perturbations of the Interplanetary Magnetic Field by the Lunar Wake," JGR, 73, 11 (1968).

15 - Parkhomenko, E.I., "Electrical Properties of Rocks," Plenum Press (1967).

16 - Reynolds, R.T., P.E. Fricker and A.L. Summers, "Effect of Melting Upon Thermal Models of the Earth," JGR, 71, 579 (1966).

17 - Rikitake, T., "Electromagnetism and the Earth's Interior," Elsevier Press (1966).

18 - Runcorn, S.K. and D.C. Tozier, "The Electrical Conductivity of Olivine at High Temperatures and Pressures," Ann. Geophys. 11, 98-102 (1955).

19 - Shankland, T.J. "Band Gap of Forsterite," Science, 161, 51 (1968).

20 - Siscoe, G.L., E.F. Lyon, J.H. Binsack and H.S. Bridge, "Experimental Evidence for a Detatched Lunar Compression Wave," JGR, 74, 59, (1969).

21 - Sonett, C.P. and D.S. Colburn, "Establishment of a Lunar Unipolar Generator and Associated Shock and Wake by the Solar Wind," Nature, 216, 340 (1967).

22 - Sonett, C.P. and D.S. Colburn, "The Principle of Solar Wind Induced Planetary Dynamos," Earth and Planetary Interiors, Vol. 1, 326 (1968).

23 - Sonett, C.P., D.S. Colburn and R.G. Currie, "The Intrinsic Magnetic Field of the Moon," JGR, 72, 5503 (1967).

24 - Sonett, C.P., D.S. Colburn and K. Schwartz, "The Motional Voltmeter," JGR, 73, 6601 (1968).

25 - Turkevich, A.L., E.J. Franzgrote and J.H. Patterson, "Chemical Analysis of the Moon at the Surveyor V Landing Site," Science, 158, 635 (1967).

26 - Weber, E.J. and L. Davis, Jr., "The Angular Momentum of the Solar Wind," Ap. J., 148 217 (1967).

27 - Whang, Y.C. and H.E. Taylor, "Theoretical Study of the Plasma and Fields in the Lunar Wake," Paper P54 49th Annual Meeting American Geophysical Union April 9, 1968.

28 - Wolf, R.A., "Solar Wind Flow Behind the Moon," JGR, 73, 4281 (1968).

CAPTIONS OF FIGURES

1. The electrical conductivity based upon Eqs. (12a, b, c, d) graphed both for temperature and inverse temperature. Shown are the four functions used (modified diabase not shown as it is merely scaled downwards from diabase by a factor of ten) which are taken from the references given in the text. They are chosen to give a representative range of potential conductivities to represent the moon in view of lack of better data. The slope is given by E_o/k and the intercept (at $1/T = 0$, not shown) defines σ_o.

2. Model 5 thermal profile for the whole moon after Fricker, Reynolds and Summers (1967).

3. Expanded view of thermal model profiles for the moon following Fricker, Reynolds and Summers (1967). The numerical labeling follows their paper and is discussed in the text.

4. Crustal electric field in the equatorial plane ($\theta = \pi/2$) of the moon calculated for olivine conductivity and the four thermal profiles of FRS. Only the outer 12 km under the surface is shown. Models 7 and 8 provide identical field profiles in this representation.

5. The polar ($\theta = 0$) electric field for olivine and the four FRS thermal models. Values are shown to 10 km depth. Field values along the polar direction are larger by several orders than the equatorial field due to the deposition of polarization charges. The crossing of all three curves at a depth of 2.5 kilometers is discussed in the text. The electric field for profile 6 produces the largest value for the electric field. This profile has the largest gradient in the temperature near the lunar surface.

6. Electric field vs. depth in the equatorial plane of the moon ($\theta = \pi/2$) using thermal Model 5 and the four conductivity functions. Example 1 corresponding to peridotite shows the depression of boundary field due to the large k factor resulting in a decrease of the effective motional electric field in space. Examples 2, 3 and 4 are diabase, basalt-diabase and olivine respectively.

7. The polar field ($\theta = 0$) for the Model 5 thermal profile and four conductivity functions. Peridotite is depressed as in the equatorial case for the same reason as given in Figure 6.

8. Electric field vs. depth in the equatorial plane of the moon ($\theta = 0$) and above the pole ($\theta = \pi/2$) using thermal Model 5 and the diabase ($\sigma_o = 10^3$) and modified diabase ($\sigma_o = 10^2$) conductivity functions. Because of the small k factors the fields are indistinguishable for the two different conductivity functions. The near constancy of the temperature in the deep interior produces an almost constant electric field out to almost 1400 kilometers.

9. Current density ($\vec{J} = \sigma\vec{E}$) in the equatorial plane of the moon ($\theta = \pi/2$) and along the pole ($\theta = 0$) using thermal Model 5 and the diabase ($\sigma_o = 10^3$) and modified diabase ($\sigma_o = 10^2$) conductivity functions. The current densities for the two functions differ by the ratio of the magnitude of the conductivity (10). Although $E(\theta = \pi/2)$ increases at the surface, the current density falls off. For $\theta = 0$, the increase in the electric field is just enough to counter the decrease in the conductivity.

10. Joule heating ($\sigma\vec{E} \cdot \vec{E}$) in the equatorial plane of the moon ($\theta = 0$) using thermal Model 5 and the diabase ($\sigma_o = 10^3$) and the modified diabase ($\sigma_o = 10^2$) conductivity functions. The unusual minima at 1600 kilometers for $\theta = \pi/2$ appears to be simply a result of the rapid variation in the electric field and the current density. From

Figures 9 and 10, it can be seen that the current density along the equatorial plane begins to drop off before the extremely rapid rise of the electric field near the surface, thus producing the minimum at 1600 km.

11. The equatorial magnetic field ($I/2\pi a$) is given here as a function of k. Since (Sonett and Colburn, 1967) the k factor is related to the actual induced magnetic field by a relation of the form $k \simeq \alpha H^2$ we obtain a straight line on the log plot. Of special interest is the position of olivine and basalt-diabase on the curve. This clearly indicates the controlling feature of the surface conductivity in determining the total unipolar current.

12. Lunar electrical conductivity profiles using Thermal Model 5 and the basalt-diabase and olivine conductivity functions. The surface conductivity ($r = 1740$ km) is 6×10^{-12} and 5×10^{-13} mhos/meter for the olivine and basalt-diabase models respectively. The two curves cross at $r = 1724$ kilometers. From Figure 11, it was seen that there is a larger total current from the olivine conductivity than for the basalt-diabase model, because of the lower surface conductivity for the latter.

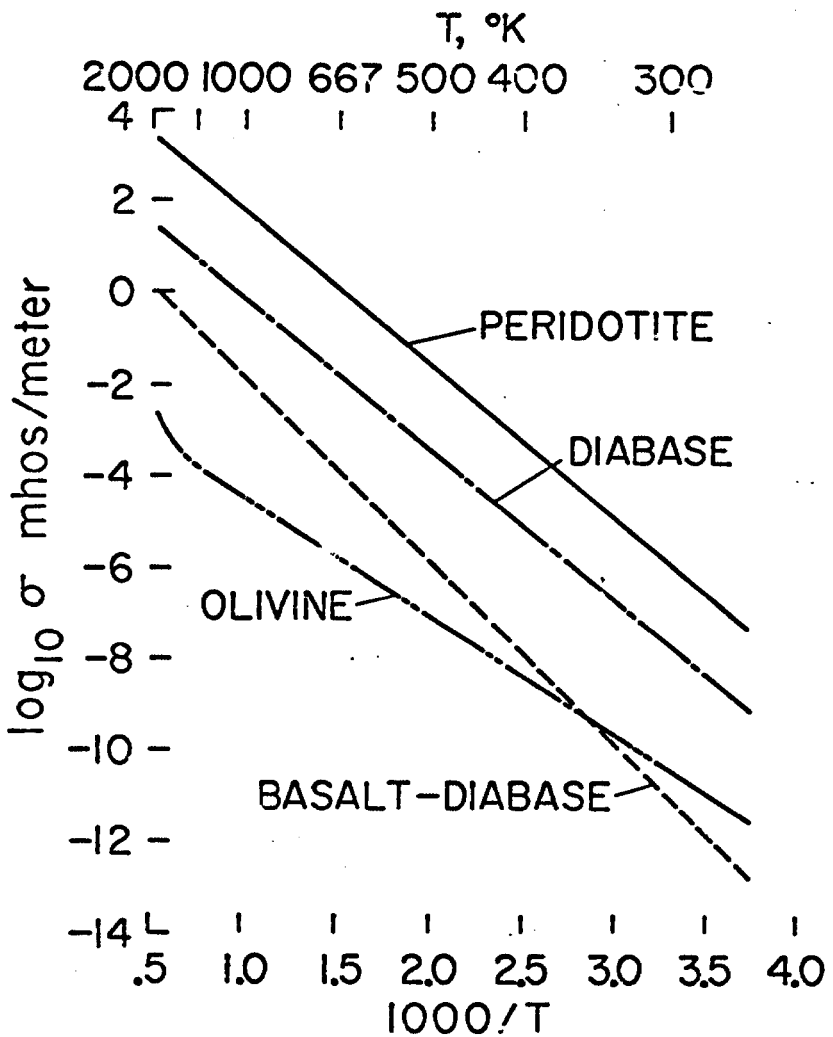

Table 1

NATIONAL AERONAUTICS AND SPACE ADMINISTRATION
AMES RESEARCH CENTER, MOFFETT FIELD, CALIFORNIA

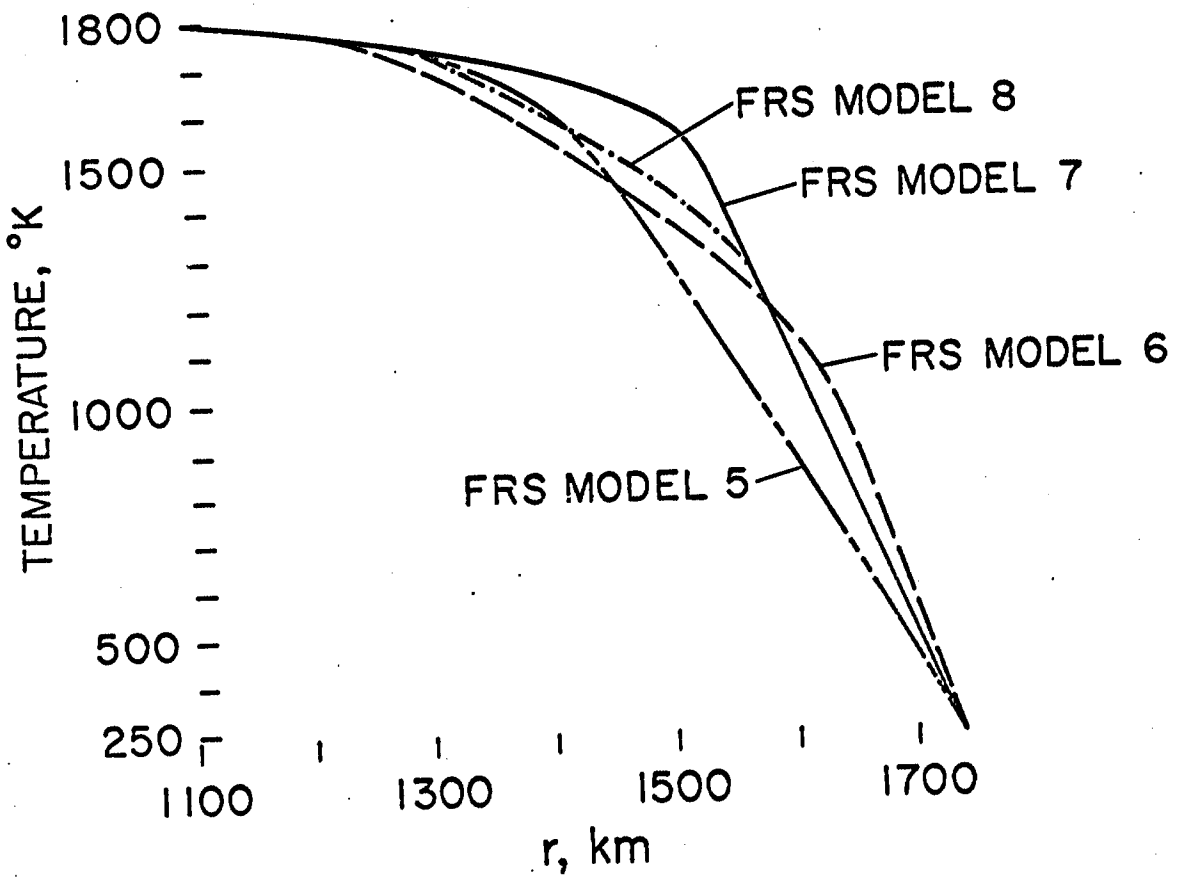

Table 3

NATIONAL AERONAUTICS AND SPACE ADMINISTRATION
AMES RESEARCH CENTER, MOFFETT FIELD, CALIFORNIA

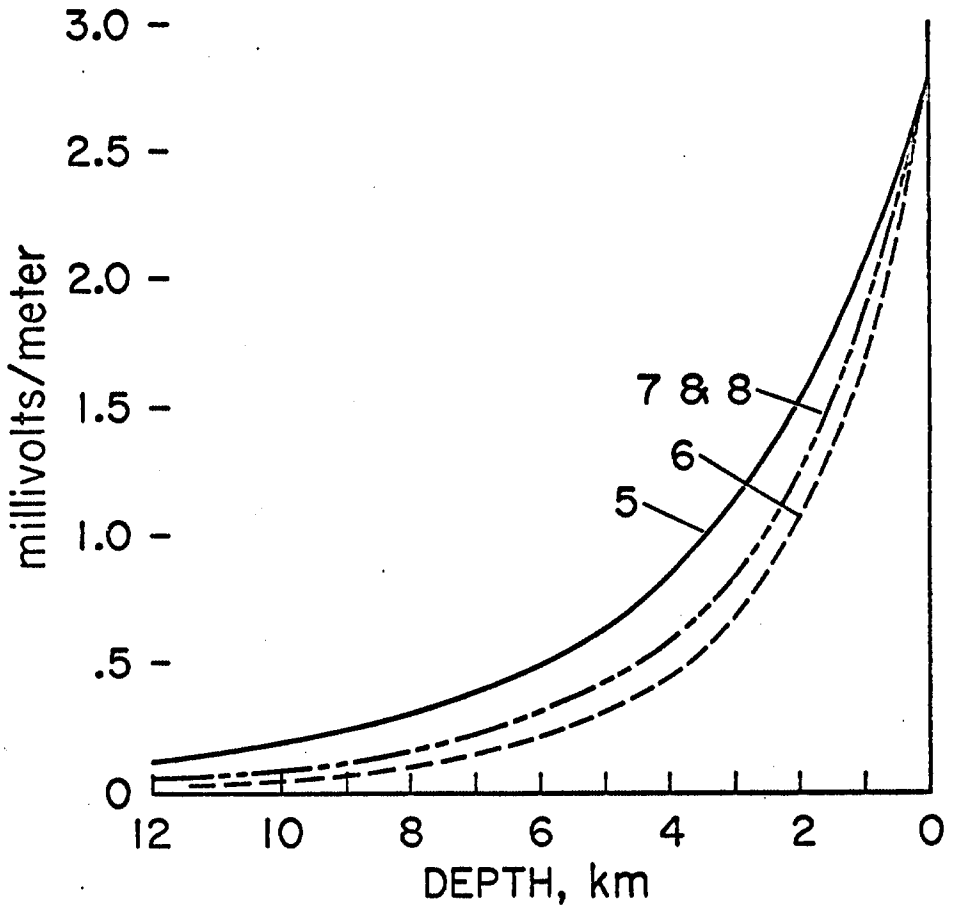

Table 4

NATIONAL AERONAUTICS AND SPACE ADMINISTRATION
AMES RESEARCH CENTER, MOFFETT FIELD, CALIFORNIA

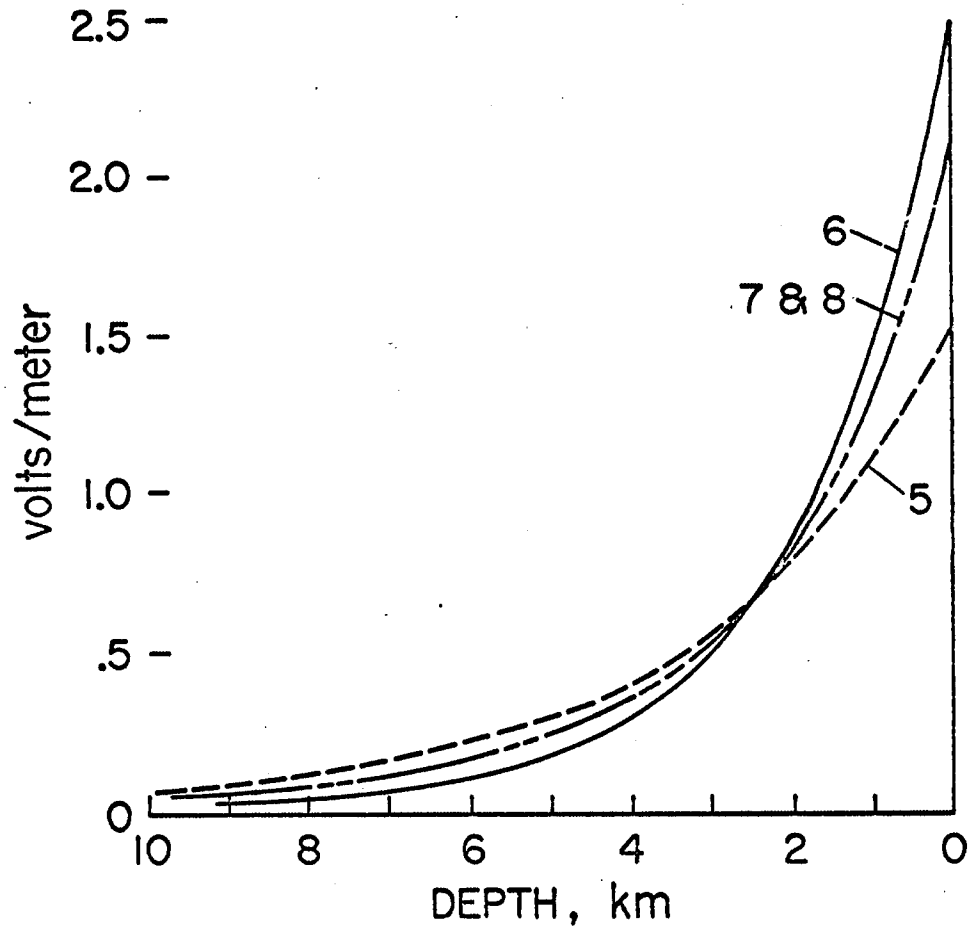

Table 5

NATIONAL AERONAUTICS AND SPACE ADMINISTRATION
AMES RESEARCH CENTER, MOFFETT FIELD, CALIFORNIA

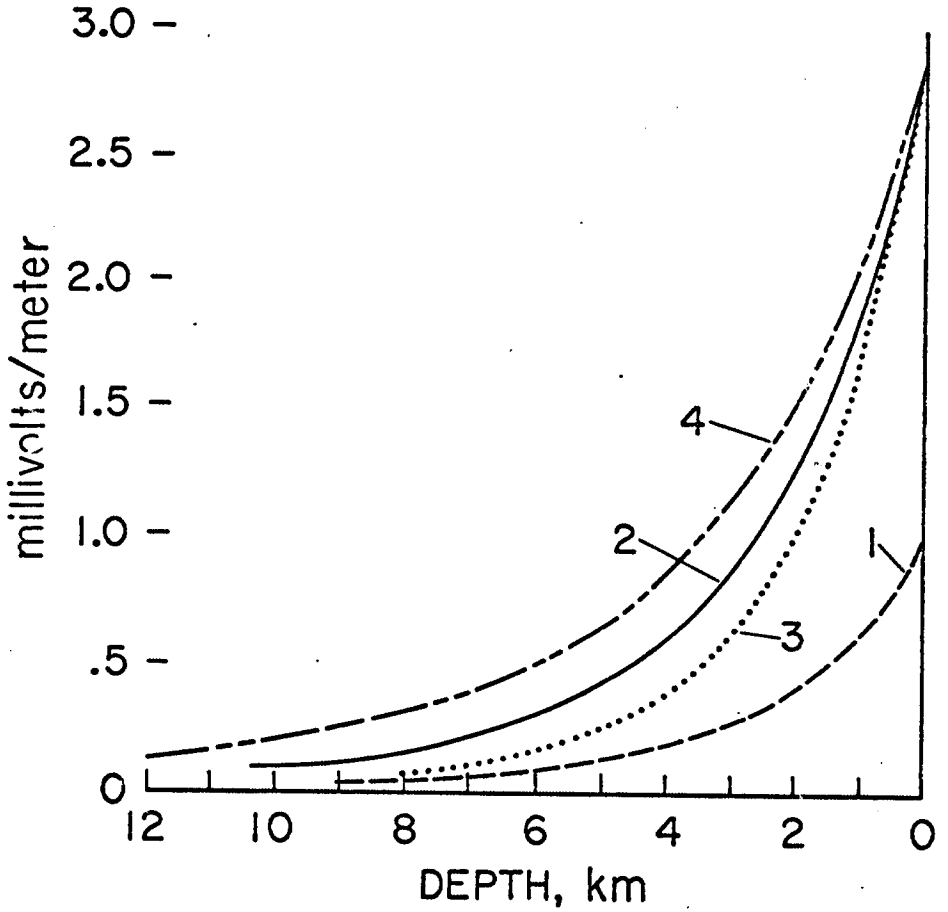

Table 6

NATION. ERONAUTICS AND SPACE ADMINISTRATION
AMES RE. ARCH CENTER, MOFFETT FIELD, CALIFORNIA

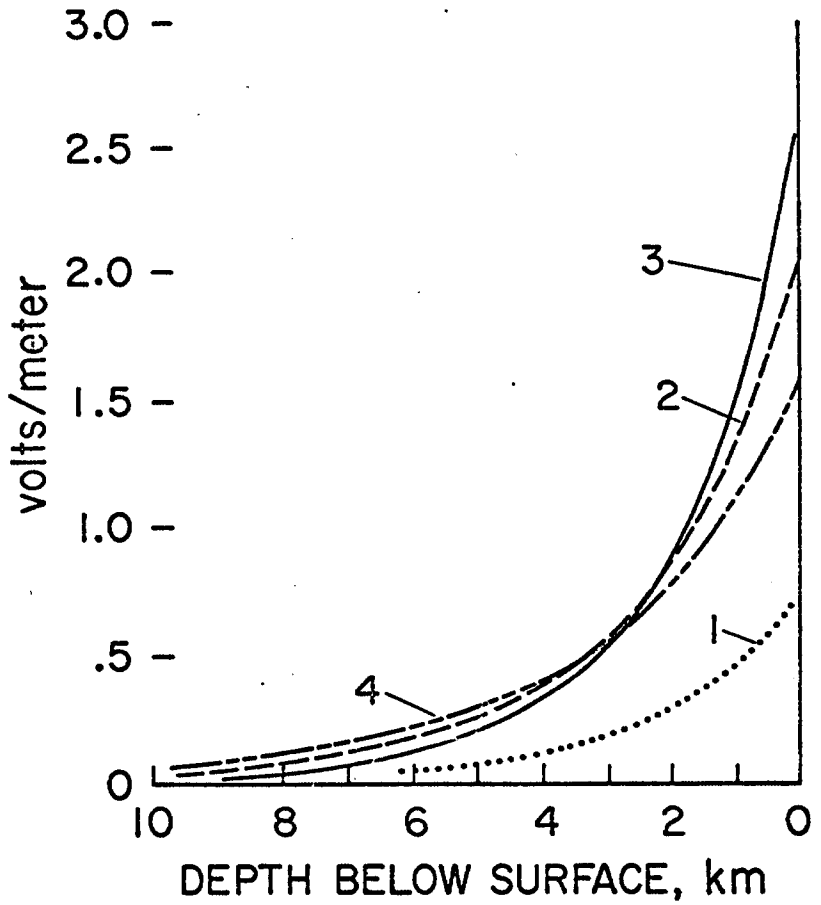

Table 7

NATIONAL AERONAUTICS AND SPACE ADMINISTRATION
AMES RESEARCH CENTER, MOFFETT FIELD, CALIFORNIA

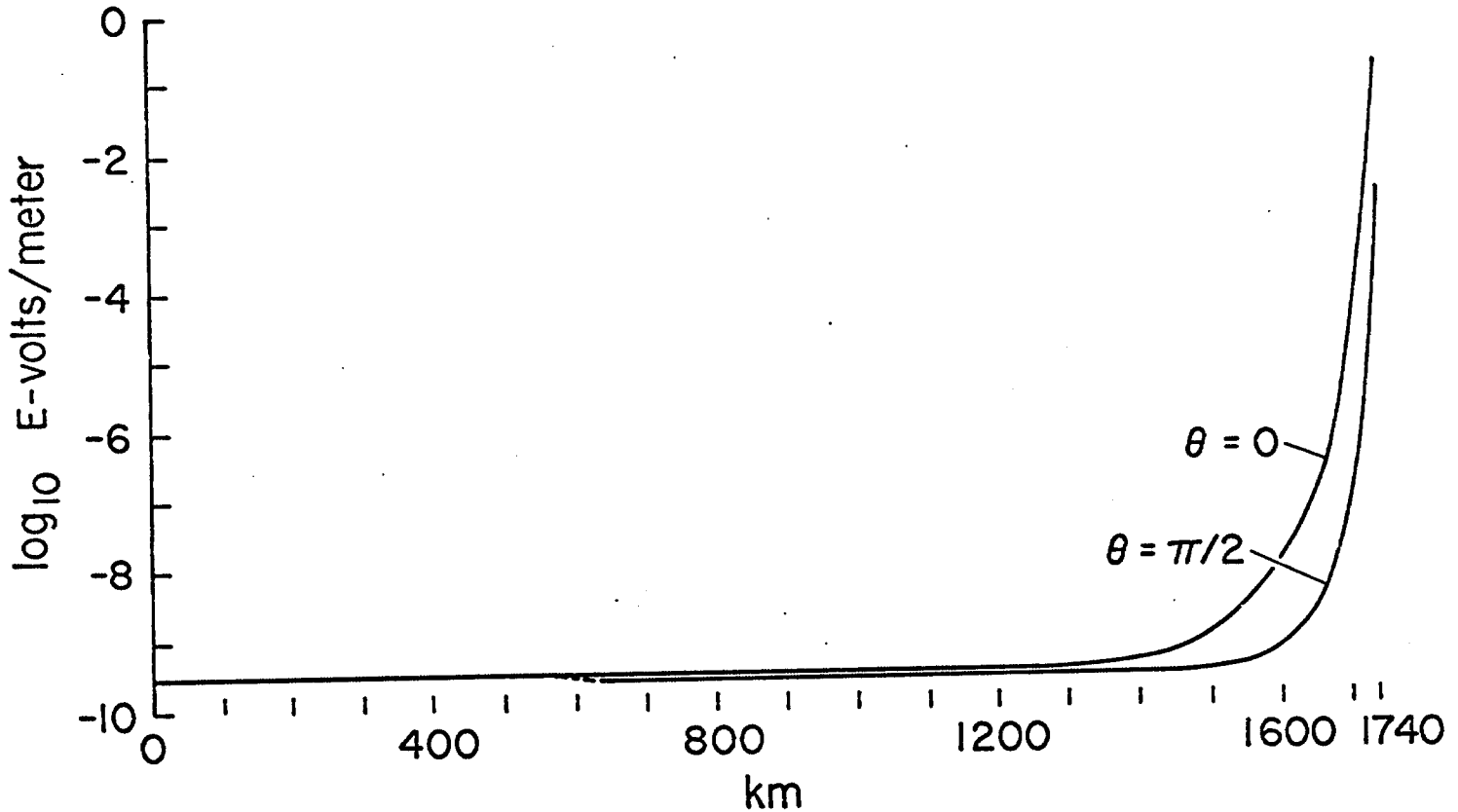

Table 8

NATIONAL AERONAUTICS AND SPACE ADMINISTRATION
AMES RESEARCH CENTER, MOFFETT FIELD, CALIFORNIA

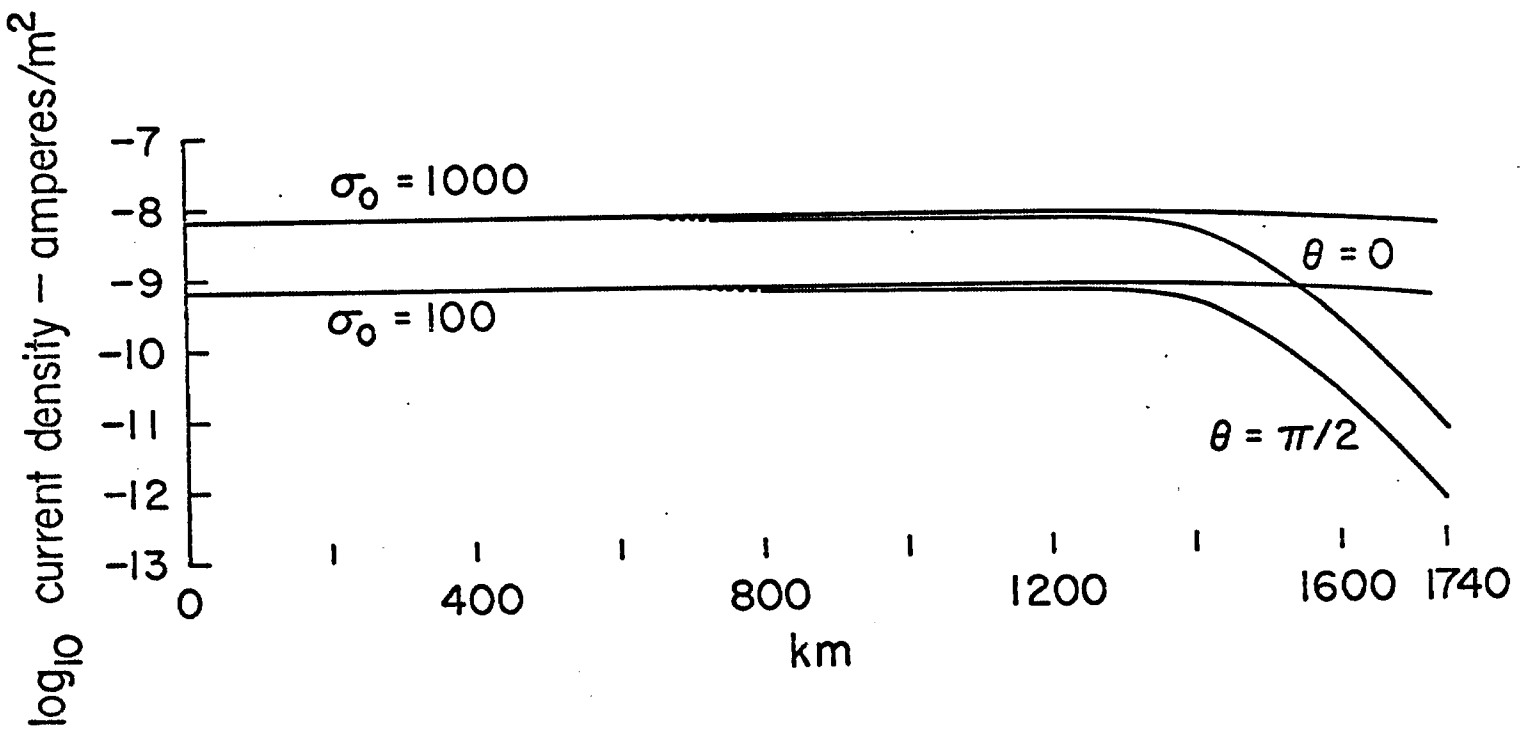

Table 9

NATIONAL AERONAUTICS AND SPACE ADMINISTRATION
AMES RESEARCH CENTER, MOFFETT FIELD, CALIFORNIA

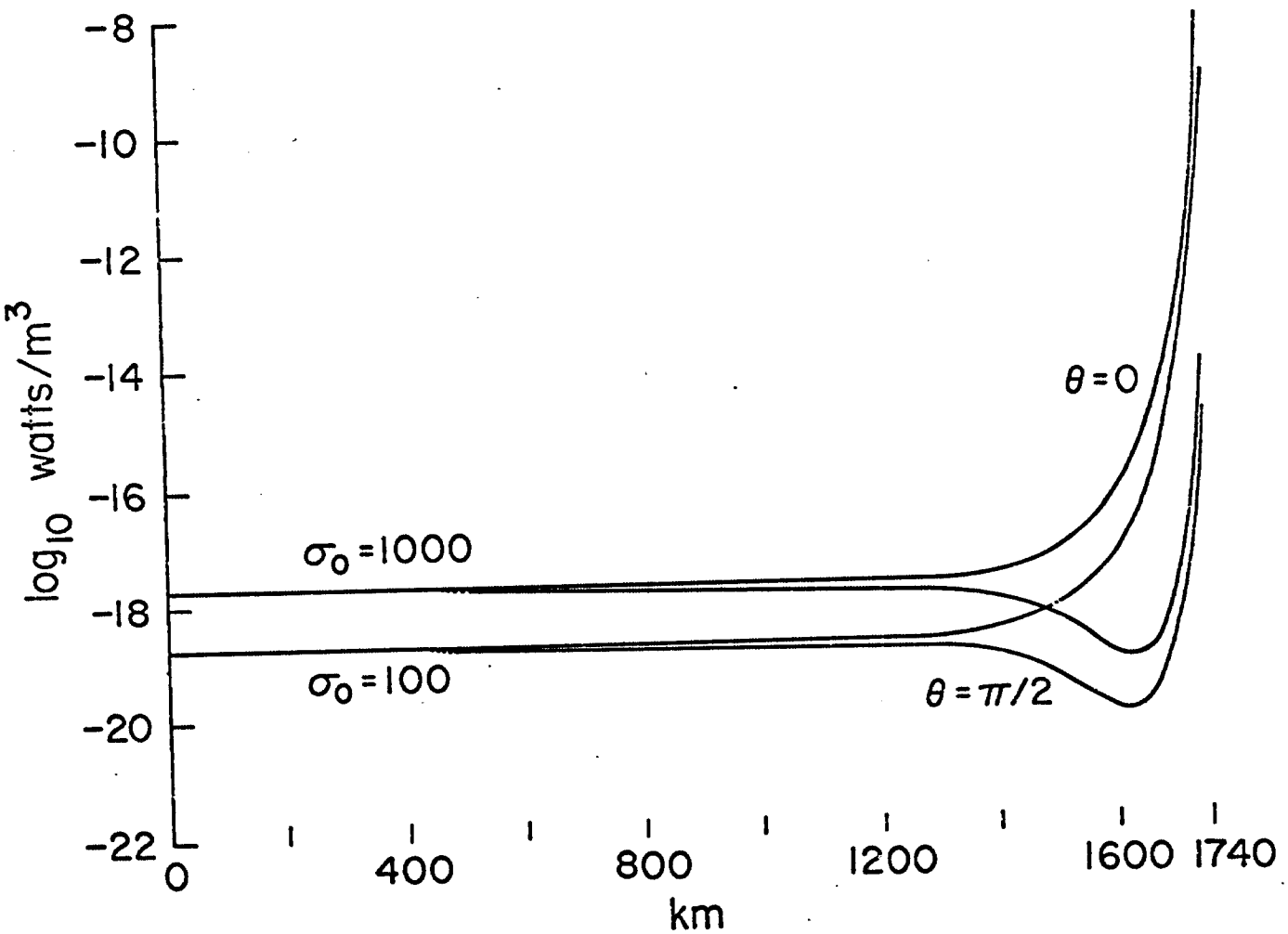

Table 10

NATIONAL AERONAUTICS AND SPACE ADMINISTRATION
AMES RESEARCH CENTER, MOFFETT FIELD, CALIFORNIA

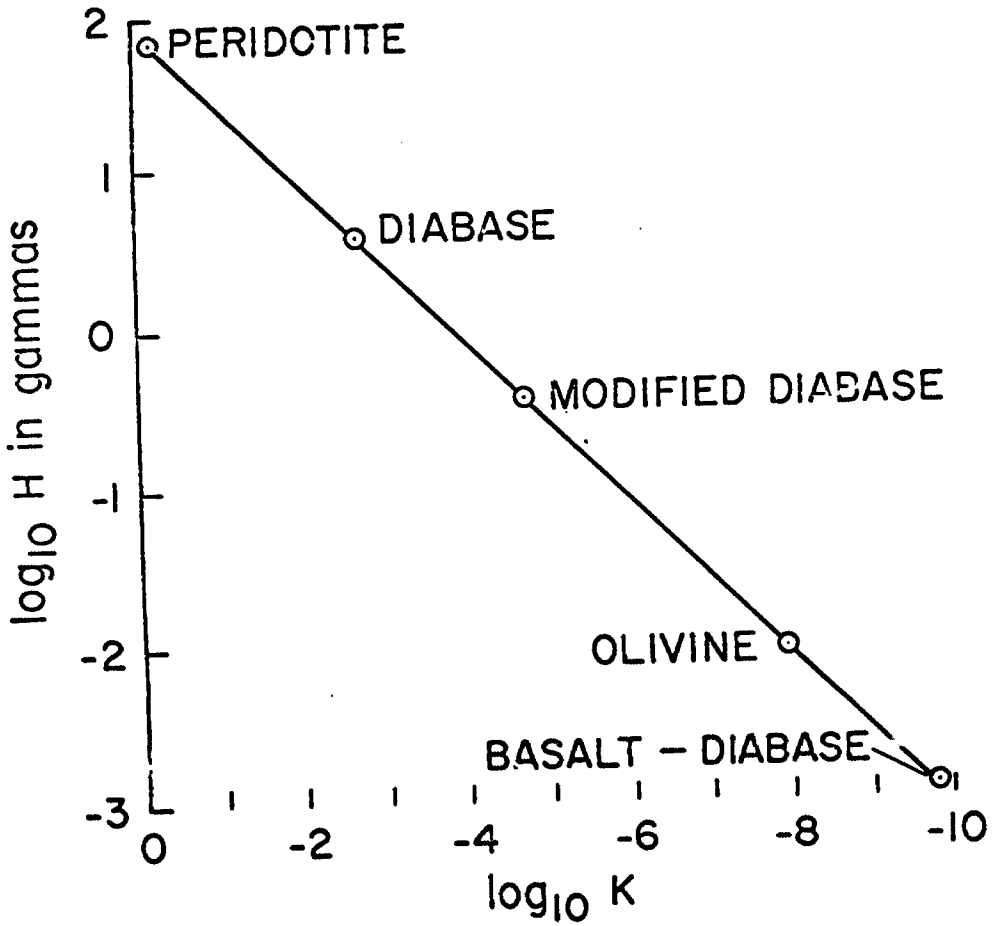

Table 11

NATIONAL AERONAUTICS AND SPACE ADMINISTRATION
AMES RESEARCH CENTER, MOFFETT FIELD, CALIFORNIA

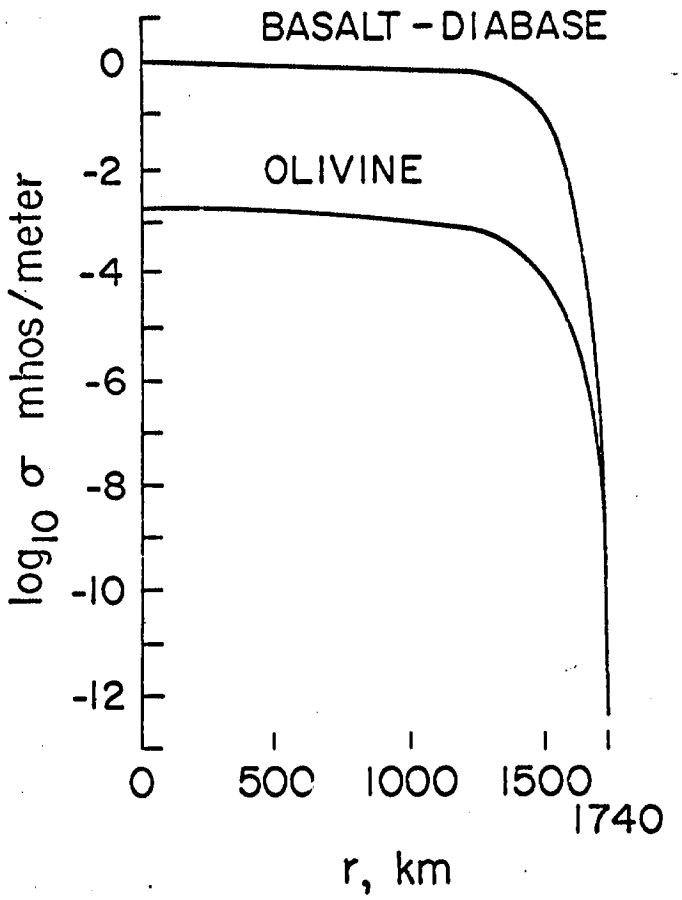

Table 12

NATIONAL AERONAUTICS AND SPACE ADMINISTRATION
AMES RESEARCH CENTER, MOFFETT FIELD, CALIFORNIA